particles

MDPI

Article

Controlling Proton Acceleration with Advanced Gold Nanoantennas in a Kinetic Plasma Environment

Konstantin Zsukovszki [1,*] and Istvan Papp [1,2,3,*]

[1] HUN-REN Wigner Research Centre for Physics, 1121 Budapest, Hungary
[2] HUN-REN Centre for Energy Research, 1121 Budapest, Hungary
[3] Sleep and Brain Plasticity Centre, Department of Neuroimaging, Institute of Psychiatry, Psychology and Neuroscience (IoPPN), King's College London, London WC2R 2LS, UK
* Correspondence: zhukovsk@hotmail.com (K.Z.); steve.prst@gmail.com (I.P.)

Abstract

Metallic nanoantennas are promising structures for enhancing energy transfer in high-intensity laser–matter interactions, especially in nanoplasmonic-assisted fusion. Under ultrashort laser pulses, they generate strong localized fields, modify ionization dynamics, and significantly affect charge acceleration in dense media. In this work, we present a comprehensive particle-in-cell (PIC) study of gold nanoantennas of various geometries—dipoles, planar crosses, three-dimensional crosses, and Yagi-inspired planar structures—irradiated by near-infrared femtosecond pulses at intensities at a range of ~4×10^{17}–4×10^{18} W/cm^2. The antenna structures are embedded in a dense hydrogen-rich medium, allowing us to follow electron emission, gold ionization, and proton acceleration self-consistently. Crossed and Yagi-type geometries exhibit more robust resonant behavior than dipoles, with higher field localization and greatly reduced sensitivity to incident polarization. The proton energies increase to ~200 keV at 4×10^{17} W/cm^2, and saturate around ~300 keV at a higher intensity >~4×10^{18} W/cm^2, dependent on the geometry. This happens largely due to a rapid loss of conduction electrons from the gold structures. Our results highlight Yagi-based and cross-based nanoantennas as promising resonant dopes for laser-driven energy coupling and point toward optimized multi-arm architectures for future nanofusion-target engineering applications.

Keywords: particle-in-cell method; nanoplasmonic effect; gold nanoantenna; plasma simulation

1. Introduction

High-intensity ultrashort-pulse lasers have enabled the exploration of new regimes in strongly driven plasmonic systems, dense plasma formation, and laser-driven ion acceleration. The intensities routinely reachable in contemporary facilities—10^{17}–10^{19} W/cm^2—drive electron motion at relativistic velocities, alter the dielectric response of metals, and accelerate ions to hundreds of keV over sub-micron distances. These effects are particularly relevant to inertial confinement fusion (ICF) in nanoplasmonics (see, for example, Refs. [1–6]). In this context, it is important to enhance energy absorption from the laser pulses and improve coupling between the laser energy and the fusion fuel. These aspects are of major importance for possible nuclear reactions. A complementary avenue being explored is the intentional embedding of metallic nanostructures into the ablator or fuel. A number of studies have demonstrated that resonant nanoparticles can substantially increase absorption by confining the electromagnetic energy to nanoscale hotspots [7–11]. Metallic nanorods, nanoshells, or nanoantennas thus offer a tantalizing opportunity: rather than interacting with a uniform

Academic Editor: Armen Sedrakian

Received: 31 December 2025
Revised: 24 March 2026
Accepted: 9 April 2026
Published: 11 May 2026

material, the driver pulse interacts with an engineered plasmonic environment capable of amplifying the incoming field.

However, most existing analyses of nanoantenna behavior rely on classical electrodynamics or effective permittivity models. Such descriptions are not reliable when field strengths are strong enough to tear conduction electrons from the structure, nor when electron collisions, ballistic motion, or space-charge formation become significant. It is therefore essential to use a kinetic approach in which ions and electrons are treated as particles interacting with self-consistent electromagnetic fields.

Previous studies show that antenna geometry plays a crucial role in shaping the local electromagnetic fields and in determining the electron and ion dynamics during laser–pulse interaction in doped media. Plasmonic phenomena on nanoantennas was explored in [12,13]. The field enhancement produced by nanoantennas has been demonstrated in several studies, such as those in references [14–19], and the enhanced absorption was also demonstrated in [20]. Proton energies in the presence of dipole nanoantennas were recently measured at ELI-ALPS; the enhancement of the proton energies in an antenna-doped dense UDMA dielectric medium was reported in [21]. This influenced the choice of parameters for our simulations. Furthermore, with the scope to validate our theoretical research we reproduced the experimentally measured results with fairly good margins of numerical uncertainty.

Plasmonic phenomena in spherical antennas have been studied, although in different contexts, in [22,23]. Previous studies have shown how nanoantenna shapes affect their optical properties in pure plasmonic regimes (see e.g., [14–19]). However, the impact of antenna geometry on performance remains far less understood for strong laser fields, particularly at intensities approaching and exceeding 10^{18} W/cm^2.

The investigated antenna structures follow the geometrical specifications used in the provided report and include a classical dipole, a two-dimensional cross (four-arm geometry), a three-dimensional cross (six-arm geometry), paired configurations, and two-dimensional Yagi-type antenna assemblies with multiple arms extending perpendicular the carrying rod. Our objective is to characterize how antenna geometry influences:

- Local field enhancement;
- Plasmonic lifetime under high-intensity illumination;
- Electron spill-out and gold ionization;
- Proton acceleration;
- Sensitivity to polarization and orientation.

We place particular emphasis on identifying the configurations that yield the strongest resonance and maintain the resonant behavior for the longest time under intense driving, thereby enabling stronger charge-separation fields and higher proton energies.

2. Particle-in-Cell Methodology in EPOCH

Particle-in-cell (PIC) simulations are ideally suited for studying this regime [24]. PIC captures nonlinear plasmon formation, electron spill-out, and transient charging of structures; the breakdown of bulk dielectric models; and the acceleration of ions via charge separation fields [25–27]. For nanoantenna geometries of tens to hundreds of nanometers, the PIC resolution can fully represent a resonant structure without resorting to homogenization. This paper provides an extended analysis of gold nanoantennas embedded in dense hydrogen and subjected to sub-picosecond pulses of 795 nm radiation. The PIC method, employed in EPOCH [28], excels in most aspects as it can:

- Capture electron spill-out phenomenon;
- Track microscopic particle behaviors;
- Account for particle collisions;

- Model plasmonic lifetime effects;
- Calculate near-field enhancement modifications.

The PIC in EPOCH involves the Yee staggered grid (see Figure 1) for the Maxwell solver.

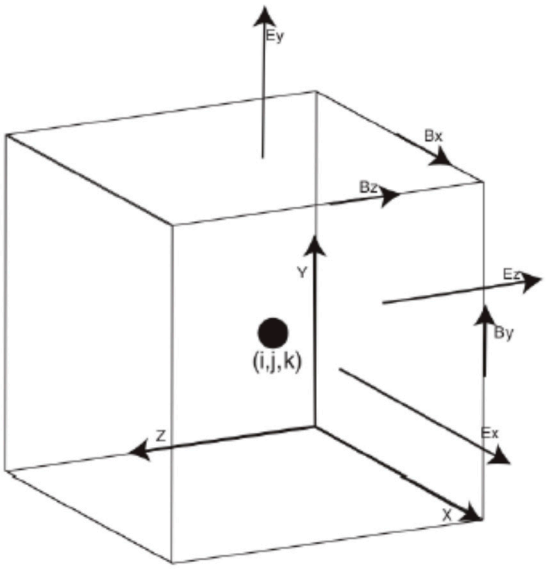

Figure 1. Yee staggered grid for the Maxwell solver in EPOCH [28].

It solves the relativistic equations of motion for charged macroparticles:

$$\begin{aligned} \mathbf{E}_{n+1/2} &= \mathbf{E}_n + \tfrac{\Delta t}{2}\left(c^2\nabla \times \mathbf{B}_n - \tfrac{\mathbf{j}_n}{\varepsilon_0}\right), \\ \mathbf{B}_{n+1/2} &= \mathbf{B}_n - \tfrac{\Delta t}{2}(\nabla \times \mathbf{E}_{n+1/2}). \end{aligned} \tag{1}$$

Furthermore, the particle pusher algorithm calculates the $\mathbf{j}_{n+1}$ current density, while advancing the electromagnetic fields via Maxwell's equations in discretized form.

$$\begin{aligned} \mathbf{B}_{n+1} &= \mathbf{B}_{n+1/2} - \tfrac{\Delta t}{2}(\nabla \times \mathbf{E}_{n+1/2}), \\ \mathbf{E}_{n+1} &= \mathbf{E}_{n+1/2} + \tfrac{\Delta t}{2}\left(c^2\nabla \times \mathbf{B}_{n+1} - \tfrac{\mathbf{j}_{n+1}}{\varepsilon_0}\right). \end{aligned} \tag{2}$$

A super particle or a marker particle in EPOCH numerical computations [25,26,28] represents many particles. Ion–electron collisions are implemented with Coulomb collisions, based on the cumulative scattering angle, proposed by Nanbu and Yonemura [29,30]. Massive gold ions remain relatively static, while conducting electrons in gold are driven toward the surface of the nanoantennas by mutual repulsion, where they are retained by the attractive field of positively charged gold nuclei and are affected by radiation, which may knock them out of the gold. The fields are defined on a staggered Yee grid. The leap-frog scheme ensures that electric and magnetic fields are updated with minimal numerical dispersion. The Boris method [31] particle pusher is used for particle advancement. Its simplistic nature is crucial for modeling high-amplitude oscillatory electron motion, preventing unphysical energy growth in the conduction electron cloud surrounding the gold antenna. It solves the relativistic equation of motion for each marker particle with the Lorentz force calculation:

$$\mathbf{p}_{n+1} = \mathbf{p}_n + q\Delta t[\mathbf{E}_{n+1/2}(\mathbf{x}_{n+1/2}) + \mathbf{v}_{n+1/2} \times \mathbf{B}_{n+1/2}(\mathbf{x}_{n+1/2})], \tag{3}$$

where $\mathbf{p}$ is the particle momentum, q is the particle charge, $\mathbf{v}$ is the velocity, and $\mathbf{p} = \gamma m\mathbf{v}$, where m is rest mass $\gamma = [(\mathbf{p}/mc)^2 + 1]^{1/2}$.

Current calculation in EPOCH is performed using the Villasenor–Buneman algorithm [32]. This scheme strictly preserves charge continuity: $\nabla\cdot\mathbf{E} = \rho/\epsilon_0$, where

$\varepsilon_0 = 8.854 \times 10^{-12}$ F/m is the vacuum permittivity and ρ is the charge density, which becomes particularly important as electrons are rapidly expelled from the metal structure and form thin sheath regions. The second-order particle shape function used in EPOCH is schematically demonstrated in Figure 2.

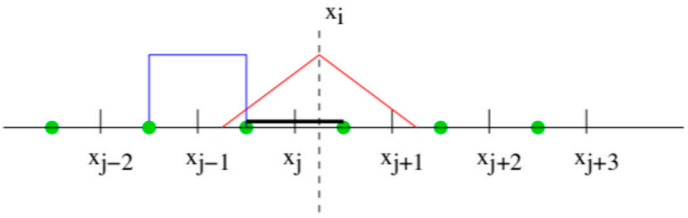

Figure 2. Second-order particle shape function. Green dots mark the cell centres, while the dashed line marks the virtual centre of a marker-particle.

For calculating current densities, the Villasenor and Buneman scheme [32] is used, which involves the following equation (see also EPOCH manual in [28]):

$$F_{part} = \frac{1}{2}F_{i-1}\left(\frac{1}{2} + \frac{x_i - X}{\Delta x}\right)^2 + \frac{1}{2}F_i\left(\frac{3}{4} - \frac{(x_i - X)^2}{\Delta x^2}\right)^2 + \frac{1}{2}F_{i+1}\left(\frac{1}{2} + \frac{x_i - X}{\Delta x}\right)^2. \quad (4)$$

Grid size and time step selection play an important role here too. The Courant–Friedrichs–Lewy condition $C = \frac{v\Delta t}{\Delta x} \leq C_{\max}$ for multiple dimensions reads as follows:

$$C = \frac{v\Delta t}{\Delta x} + \frac{v\Delta t}{\Delta y} + \frac{v\Delta t}{\Delta z} \leq C_{\max}, \quad (5)$$

$$C = \Delta t\left(\sum_{i=1}^{n}\frac{u_{x_i}}{\Delta x_i}\right) \leq C_{\max} \quad (6)$$

where $C_{\max}$ is usually 1.

We would like to underline the differences between the kinetic PIC methods vs. traditional field solvers. While a traditional field solver involves such parameters as the material's permittivity $\epsilon(\omega)$, based on the Drude basis equation:

$$\varepsilon(\omega) = 1 - \frac{\omega_p^2}{\omega^2 + i\gamma\omega}, \quad (7)$$

and Maxwell equations:

$$\frac{\partial \mathbf{E}}{\partial t} = \frac{1}{\mu_0\varepsilon_0}\nabla \times \mathbf{B} - \frac{\mathbf{J}}{\varepsilon_0}. \quad (8)$$

The kinetic model explicitly simulates particle dynamics using relativistic equations of motion

$$\gamma_i m_i \mathbf{v}_i = q_i(\mathbf{E}_i + \mathbf{v}_i \times \mathbf{B}_i), \quad (9)$$

and applies self-consistent field updates (2).

In summary, a simulation was performed in the EPOCH software package (version 4.17) environment. The computational box measured $530 \times 530 \times 795$ nm^3 and was discretized on a grid of $159 \times 106 \times 106$ cells, fine enough to resolve plasmonic oscillations and electron spill-out. The 795 nm laser shot crossed the simulation box within a single period: $T_P = \lambda/c = 2.65$ fs, and the temporal resolution amounted to one quarter of the period. Importantly, in the PIC scheme, the boundaries are defined by super-particle number density, not by dielectric function changes. Absorbing or free propagation boundary conditions are applied to fields and particles to avoid unphysical reflections. The closed

reflecting boundary conditions for particles were also tested; they yielded similar results apart from the case where the charges left the simulation box too early in a very strong laser field and the nanoantenna was large, comparable with the simulation box height. Then, the reflecting boundary preserved particles in the simulation box and allowed us to observe the final energy level after the passage of the whole length of the laser pulse.

The influence of Coulomb collisions was assessed through comparative simulations with collisions disabled. Collisions were found to modestly reduce electron spill-out and prolong plasmon lifetime, while maximum proton energies differed by less than 10%. In the present relativistic regime, collisions mainly influence electron thermalization and have a secondary impact on the dominant field-driven acceleration mechanism.

A numerical convergence study was performed for a representative dipole antenna configuration by varying grid resolution, time step, and number of macroparticles per cell. The time step was determined from the Courant stability condition, ensuring accurate relativistic field propagation and numerical stability. Convergence tests with varying grid spacing and macroparticle number showed variations below ~10% in peak fields and proton energies. The peak near-field amplitude and maximum proton energy were found to converge within the range of 5–8% for grid spacings below 5 nm and macroparticle numbers exceeding 50 per cell. All simulations reported in this work were performed within this converged parameter regime.

3. Antenna Kinetic Modeling and Local Field Enhancement

Conduction band electrons behave as strongly coupled plasma. The resonating wavelength λ_0 for a $D = 2R = 25$ nm diameter gold nanorod in vacuum is ≈270 nm as follows from the analytical estimate in [33]:

$$\frac{\lambda_0}{2R\pi} = 13.74 - 0.12[\varepsilon_\infty + 141.04] - \frac{2}{\pi} + \frac{\lambda}{\lambda_p} 0.12\sqrt{\varepsilon_\infty + 141.04}, \quad (10)$$

where λ_p is the plasma wavelength. But in dense dielectric media, the resonance length of a dipole is no more than $\lambda_0/2$; it depends on the refraction coefficient of media $n = \sqrt{\varepsilon}$. The effective resonance plasmonic wavelength λ_{eff} is not the free-space wavelength λ_0. It is $\lambda_{eff} = 2L_{eff}n_{eff}$, where n_{eff} is the effective refractive index of the plasmon mode, which depends on the permittivity $\varepsilon(\lambda)$ of the surrounding medium. Straightforward use of (10) of a dielectric media where $n = 1.5$ yields the antenna length $L \approx \lambda_0/2n \approx 89$ nm, which is the correct value, though incorrectly obtained, as (10) is applicable in a vacuum for long, thin antennas $R << L$, $R << \lambda$. However, $\lambda_0 \propto R$ in (10) and even in the stated range of applicability yields an unphysical result: $\lim_{R\to 0}\lambda_0 = 0$. Moreover, when using the value proposed in [33] in the "corrected" form of (10) for dense media, for $\varepsilon = 2.25$ and $R \approx 0.15L$, we get wrong estimated rod length 30 nm, which clearly underestimates the actual resonance and contradicts the numerically computed resonance at λ_{eff}~170 nm, reported earlier in [19]. In practice, the resonant wavelength is determined by the antenna length, environment refractive index, and mode dispersion, accurately captured by full electromagnetic simulations of I. Papp in [19] and other works.

A valid analytical approach is based on an effective resonant length $\lambda_{eff} = \lambda_0/n_{eff}$, where n_{eff} is the effective refractive index of the plasmon mode. It determines the effective resonating length of the rod $L_{res} \approx \lambda_{eff}/2$. From the experimental data for gold at 800 nm, its dielectric function has an approximate value of $\varepsilon \approx -24.5 + 1.8i$ [34]; for a gold nanorod in dense media where $n = 1.5$, the effective refractive index is $n_{eff} \approx 4.5$–6.0 [34]. The effective resonant wavelength $\lambda_{eff} = \lambda/n_{eff}$ for the laser vacuum wavelength (800 nm) becomes $\lambda_{eff} \approx 133$–$178$ nm, where media have been already accounted for. This means that the resonant half-length is $L_{res} \approx 66$–89 nm for the laser at 800 nm.

In our study, we investigate the following prominent antenna shape configurations:

- Dipole nanorods with length ~85 nm and diameter ~25 nm, chosen near the resonant length of gold in a medium with a refractive index of ~1.5.
- Planar crosses with two perpendicular nanorods intersecting at the center.
- 3D crosses with three perpendicular nanorods intersecting at the center.
- Yagi-inspired symmetric antennas, formed by adding dipoles in both directions across the connection rod, analogous to directors in RF Yagi antennas.

Each structure is resolved fully in the grid. The antenna in its simplest dipole form is modeled by a rod with a 25 nm diameter and 85 nm length. The surrounding medium around the antenna in the simulation box is dense atomic hydrogen, chosen for its simplicity and relevance to fusion environments. Ionization is modeled dynamically: electrons detach from hydrogen upon exposure to strong fields, forming plasma of electrons and protons.

Charge conservation was verified by monitoring Gauss's law during the simulations, with deviations remaining within the level typical for relativistic PIC simulations using the chosen numerical parameters.

Gold was modeled with three conduction electrons per ion, reflecting its valence electron structure. These mobile electrons represent the plasmonic electron gas responsible for resonant oscillations. Once expelled from the nanoantenna, the gold core becomes positively charged and subsequently undergoes further field-driven ionization. At the highest intensities, deeper ionization stages may develop; however, plasmon decay is mainly governed by relativistic electron escape from the antenna, making the qualitative trends largely insensitive to the exact ionization stage.

The simulation involved five species of charges: H atoms, Au^{3+}, Au electrons, H ions–protons, and H electrons appearing during ionization.

The simulations used a near-infrared laser pulse with the following characteristics:

- Wavelength: 795 nm.
- Duration: ~120 fs (98 fs flat top with smooth 10 fs ramps at endpoints).
- Peak intensity: 4×10^{18} W/cm^2.
- Polarization: linear, user-selectable, and variable polarization.
- Propagation: along the long axis of the simulation volume.

The beam waist was chosen such that the antenna fully experienced the high-field region.

In our study, upon modeling the laser field–matter interaction, we noted early-time plasmon formation. Within the first ~20–30 fs range of the pulse, conduction electrons in gold showed coherent oscillations. In dipole rods, these oscillations occur primarily along the long axis. In crossed and Yagi-type geometries, multiple oscillation pathways exist, enabling several hotspot regions to form simultaneously. To illustrate the dynamics of the conducting charges, snapshots of the electric field and electron number density evolution around a nanorod are presented in Figures 3 and 4, respectively.

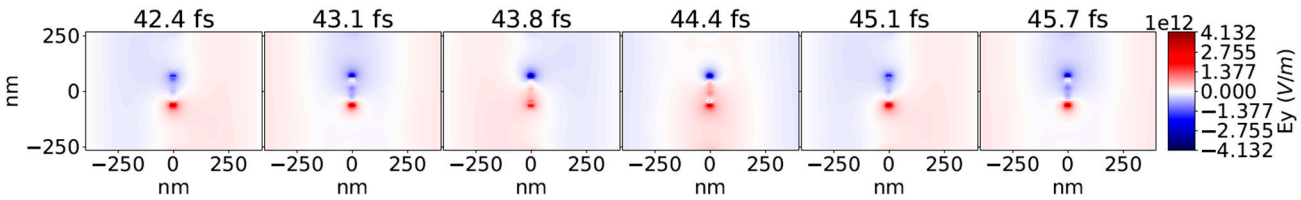

Figure 3. Electric field around a dipole nanoantenna positioned perpendicular to the irradiation direction x. Moments in time show the evolution of the electric field around the antenna.

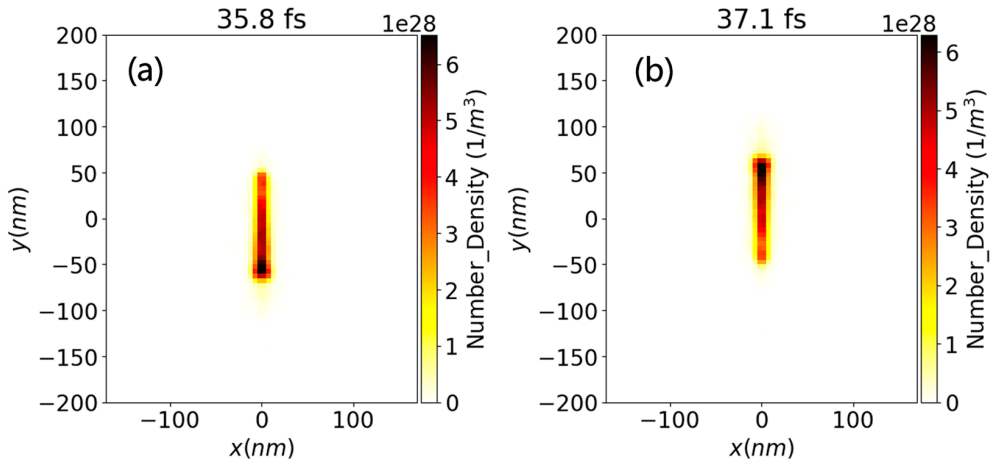

Figure 4. Conducting electron number density on a dipole nanoantenna positioned perpendicular to the irradiation direction x at close time moments: 35.8 fs (**a**) and 37.1 fs (**b**). Asymmetric distribution of electron density along dipole indicates surface plasmon on the gold antenna. Difference between plots in (**a**,**b**) indicates the evolution of the electron number density corresponding to oscillations of the surface plasmon on the gold nanodipole.

Numerical modeling expectedly reveals that dipole rods are highly orientation dependent. A mismatch of the orientation angle between the polarization and rod axis reduces the field enhancement. In contrast with a dipole, crossed antennas maintain strong responses essentially in any orthogonal plane orientation, while 3D crossed assemblies maintain it in all three spatial dimensions. This reduced sensitivity is particularly important in realistic ICF environments, where multi-beam irradiation introduces variations in both the angle and polarization. Cross-shaped antennas show substantially stronger local field enhancement, with amplitudes exceeding those of the incident field by more than an order of magnitude. Yagi-type and 3D-based geometries, containing multiple arms, have additional current paths. They exhibit intense hotspot regions located near the rod terminations. These hotspots support more robust plasmonic formation and are responsible for the enhanced localized ionization of hydrogen and for the proton acceleration. This is confirmed by energy performance analysis, which also demonstrates that the 2D cross-quadruple has an optimal dipole performance, while providing consistent energy deposition across orientations, and a superior performance is maintained at higher intensities.

Analyses of electron emission and gold ionization show that strong localized fields efficiently remove conduction electrons from the gold antennas. Within a range of 40–60 fs, a significant fraction of the conduction electron cloud escapes into the surrounding medium. This spill-out generates positive charge buildup on the gold ion core, a transient electron sheath, and a rapidly changing local dielectric environment.

Dependence on laser intensity has been addressed in an array of simulations for a variety of antenna geometries in the fields, whose intensities ranged from 10^{15} to 10^{19} W/cm^2. Importantly, at 4×10^{17} W/cm^2, a substantial number of conduction electrons remain for roughly half the pulse duration, allowing the antennas to maintain resonant behavior during the pulse duration. This may be associated with plasmon lifetime, and it is shorter for dipoles than for cross-based antennas, especially 3D crosses. In contrast, at high field intensities $>2 \times 10^{18}$ W/cm^2, conduction electrons are expelled much earlier (~20–30 fs), leading to the premature loss of plasmonic resonance. This imposes a fundamental impact on the near-field enhancement by the antennas. Once conduction electrons are depleted, the structure no longer supports large resonant currents. Field enhancements collapse rapidly, and additional field amplification becomes limited. Cross structures, in contrast to

simple dipoles, delay this collapse relative to dipoles because distributed currents require more time to remove enough electrons to break the resonant pathway.

While isolated antennas establish a baseline plasmonic response, the introduction of neighboring structures enables hybridization effects that can substantially modify near-field dynamics and energy transfer.

4. Reference Simulation Without an Antenna

To isolate nanoantenna-induced effects from conventional laser–plasma interaction and acceleration, a reference simulation without antennas was performed under identical laser and plasma conditions in hydrogen-rich matter. In this configuration, ionization and proton acceleration are driven solely by the laser field. Visualization and analysis of the results were performed with a third-party application: Visit version 3.0.3 [35].

The results depend on the laser intensity. For a high-intensity 4×10^{18} W/cm^2 laser, only a small fraction of protons has a maximum energy of >0.6 keV; protons in ~90% of the simulation volume have energy values <0.25 keV (see Figure 5). These reference results demonstrate that conventional laser–plasma interactions under identical conditions produce only weak proton acceleration, providing a baseline for assessing antenna-mediated effects.

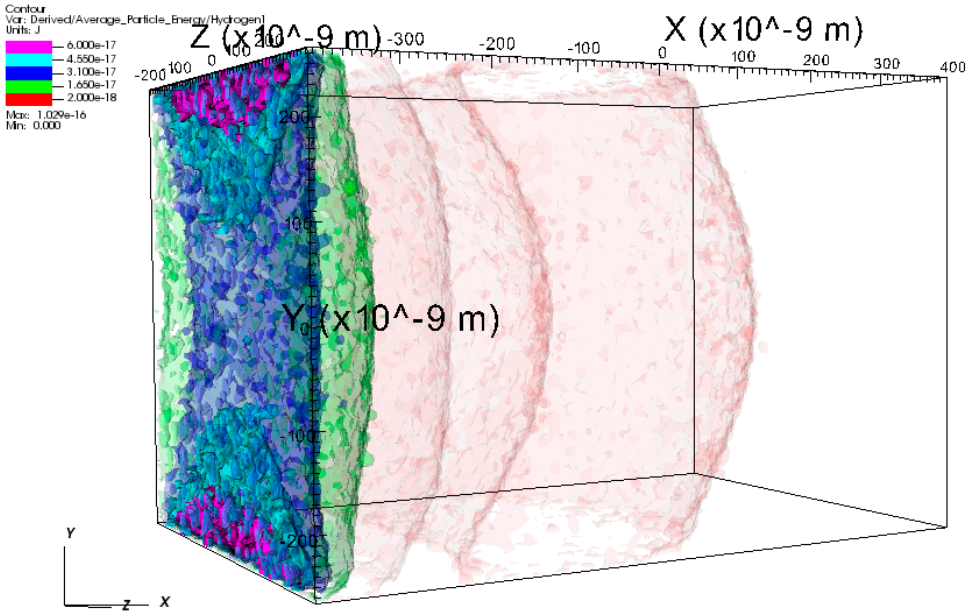

Figure 5. Space distribution of proton energies in a simulation box without nanoantennas subjected to a 4×10^{18} W/cm^2 laser pulse at ≈25 fs. Peak proton energies ≈ 0.6 keV; for most protons, $E_p < 0.2$ keV. The axis values are in [nm]; the proton energy values are in [J].

Ionization in the absence of nanoantennas occurs primarily at the early stage of pulse interaction with matter. As shown in Figure 6, electron pseudoparticles (green) and protons are generated during the ionization phase. Electrons are subsequently expelled by the electromagnetic wave over several femtoseconds, while heavier protons remain in the simulation box until the end of the pulse (≈120 fs). The maximum proton density remains nearly constant, increasing slightly from ≈6×10^{21} m^{-3} at 20 fs to ≈6.5×10^{21} m^{-3} at 120 fs.

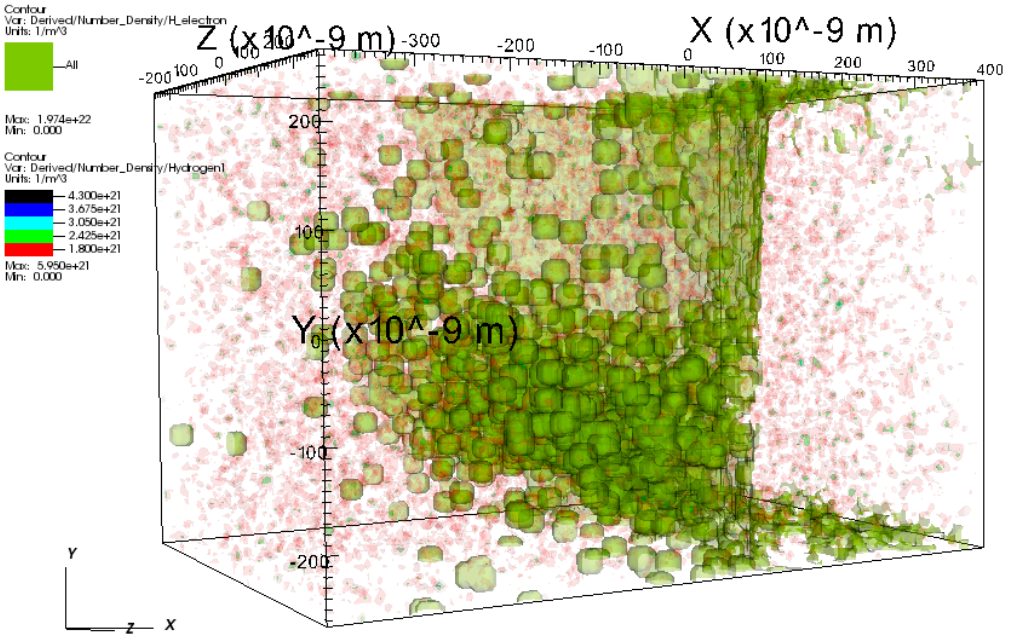

Figure 6. Number density of protons (coloured scale in legend) and electrons (green large dots) originating from hydrogen ionization by a 4×10^{18} W/cm^2 laser pulse at ≈20 fs. Peak proton density: $\approx 6 \times 10^{21}$ 1/m^3. Electrons were removed by the laser wave a few femtoseconds later. The axes values are in [nm]; the charge densities are in [1/m^3].

Without nanoantennas and for a laser intensity of 4×10^{18} W/cm^2, proton values reach:

- <0.2 keV for most protons.
- ≈0.6 keV peak proton energy.
- $\approx 6 \times 10^{21}$ m^{-3} proton number density.

This reference case therefore establishes a physically consistent baseline for evaluating antenna-induced field localization and its impact on particle acceleration.

5. Proton Acceleration and Energy Gain for Various Antenna Assemblies

The comparison with antenna-embedded configurations presented in the following section allows the specific contribution of nanoantenna-induced field localization and transient charge-separation enhancement to be quantified. The mechanism of proton acceleration arises from multiple factors, such as strong sheath fields due to ejected electrons, the Coulomb field of the positively charged gold antenna, the residual near-field enhancement from plasmonic oscillations, and the dynamic ionization fronts in the hydrogen medium. The results depend on field intensity. In moderate-intensity laser beams at 4×10^{17} W/cm^2, proton energies reach:

- ~100 keV for dipoles.
- ~180 keV for cross-based antennas.
- ~200 keV for Yagi antennas.

These differences reflect stronger and more spatially extended fields in multi-arm antenna geometries. Proton energy saturation was observed at high laser intensities. At >10^{18} W/cm^2, the proton energy rises only slightly compared to the moderate-intensity case. The final energy values of protons reached roughly:

- ~120 keV for dipoles.
- ~250 keV for cross-based antennas.
- ~300 keV for Yagi antennas.

These results indicate an enhancement of two to three orders of magnitude in peak proton energy values compared to the antenna-free case (see Section 4). Yagi antennas benefit from closely placed resonating dipole elements, while crossed-based antennas benefit from hybridized modes of their crossed arms.

The reason for the marginal improvement in the >10^{18} W/cm^2 field over 10^{17} W/cm^2 is because intense fields expelled the gold's conduction electrons early and shortened the plasmon lifetime. This eliminates the resonant enhancement that would otherwise support stronger charge-separation fields. After this point, additional intensity does not translate to stronger acceleration. The observed action of proton energy saturation with rapid electron depletion and plasmon decay is consistent with previously reported plasmon collapse mechanisms [14–18]. To illustrate this point, we compare the conduction electron density near the antenna in Figures 7 and 8 with the proton energy evolution shown in later figures.

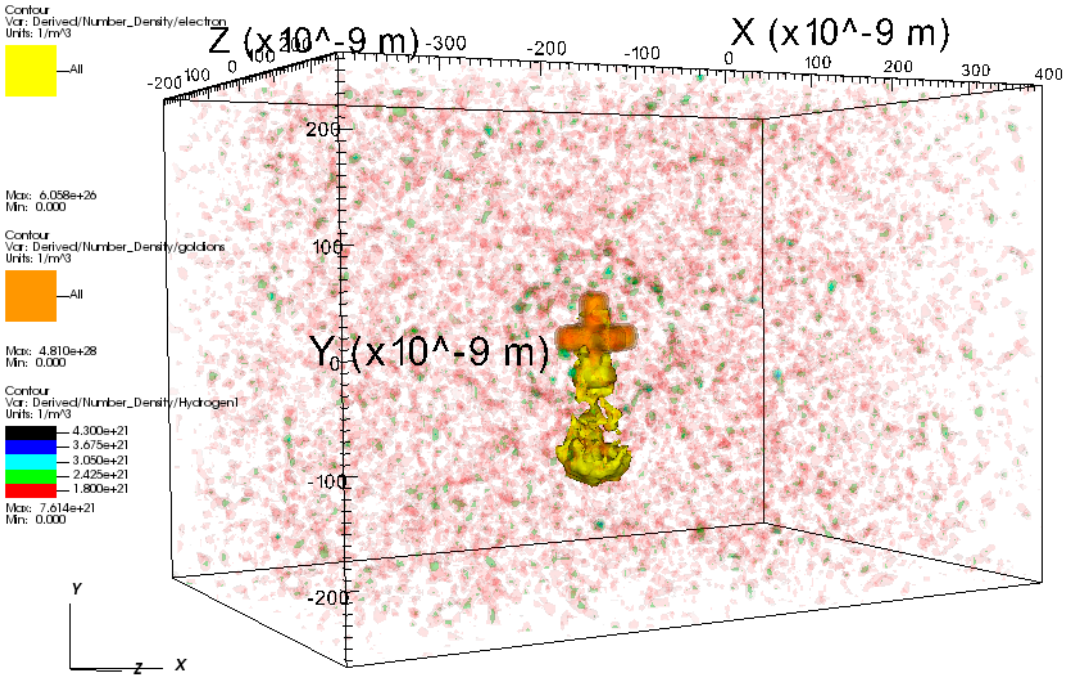

Figure 7. Space distribution of charge densities around the nanoantenna at a simulation time of ≈35 fs. Yellow conduction electrons of gold form plasmon. This is affected by the 4×10^{18} W/cm^2 laser wave. Gold ions of the antenna remain in place (orange cross). See legend for all species of charges. The axis values are in [nm]; the charge densities are in [1/m^3].

Conducting electrons (yellow) form a surface plasmon on the gold 3D crossed antenna (orange cross), shown in Figure 7. The plasmon has a high amplitude of oscillation in the 4×10^{18} W/cm^2 field and it partially detaches from the antenna at ≈35 fs (see Figure 7) as electrons are ejected. Then, the proton energy growth slows (~35 fs; see the last figure). After ≈50 fs, the gold conducting electrons are ejected (yellow dots in space in Figure 8) and carried away by the laser field. At the same time, proton energy growth further slows down. It coincides with the rapid decline in the energy of gold electrons. The electrons leave the simulation box affected by a strong laser wave, and the resource of conducting electrons in gold is depleted. This supports the interpretation that electron spill-out limits further efficient energy transfer from the wave to protons and electrons.

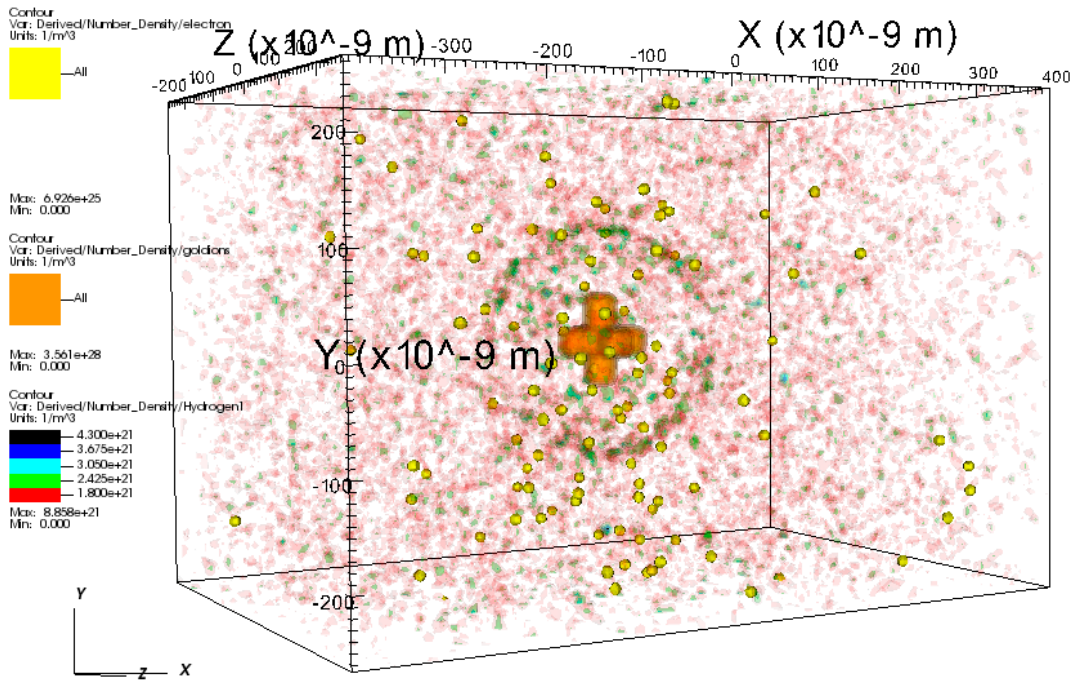

Figure 8. Space distribution of charge densities around the nanoantenna at a simulation time of ≈47 fs. Yellow conduction electrons of gold are knocked out and removed by the 4×10^{18} W/cm^2 laser wave. Gold ions of the antenna remain in place (orange cross). See legend for all species of charges. The axis values are in [nm]; the charge densities are in [1/m^3].

Moreover, the spatial distribution of the acceleration depends on the antenna shape and construction. Dipole structures generate elongated acceleration regions, while crosses produce more symmetric proton outflows. 3D-crossed antenna geometries create a broad spherical-shell-like distribution due to their three-dimensional symmetry, while Yagi-based antennas produce an elongated spatial distribution due to their geometry.

In our study, we examined a number of extended antenna configurations and multi-element antenna assemblies; some of them are shown in Figures 9 and 10.

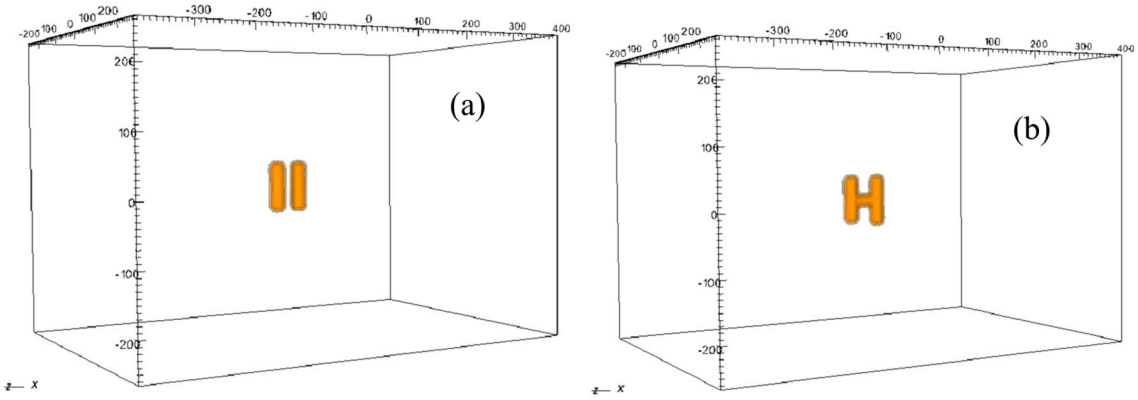

Figure 9. Coupled parallel dipole antenna; (**a**) simplest Yagi-type directed antenna (**b**).

https://doi.org/10.3390/particles9020051

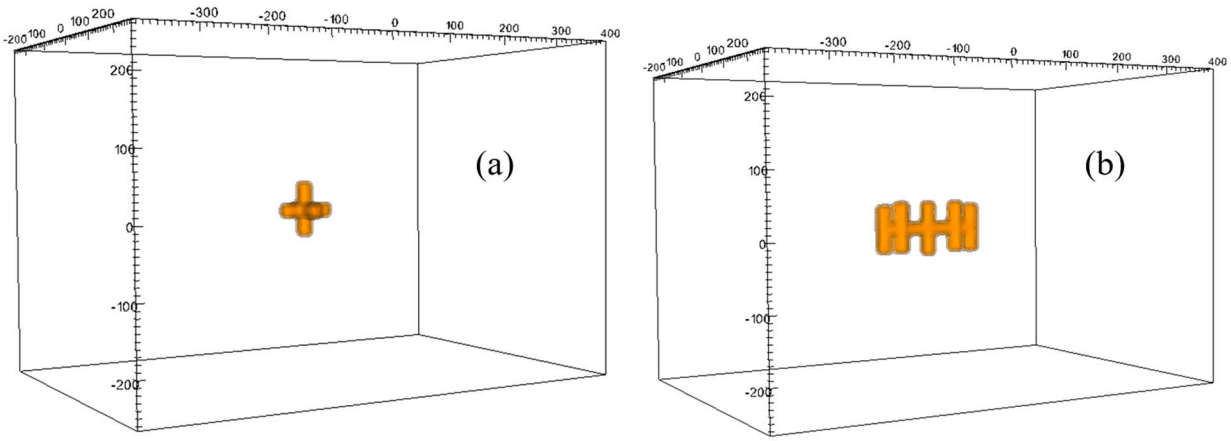

Figure 10. 3D crossed antenna (**a**); double-sided Yagi-type antenna (**b**).

We discovered that the distance between closely placed antennas matters for proton energies, as demonstrated, for example, in Figure 11. Unlike in closely spaced pairs, larger gaps between antenna elements yields weaker near-field enhancement. This can be observed in Figure 11 upon the comparison of the red dotted line, showing the maximum proton energy obtained with a pair of dipoles placed at a 42 nm distance vs. the black dot-dashed line in Figure 11, showing the maximum proton energy for a dipole pair at a distance of 85 nm. The comparison of the two lines in Figure 11 evidence that higher proton energy values can be achieved with the closer pair of dipoles.

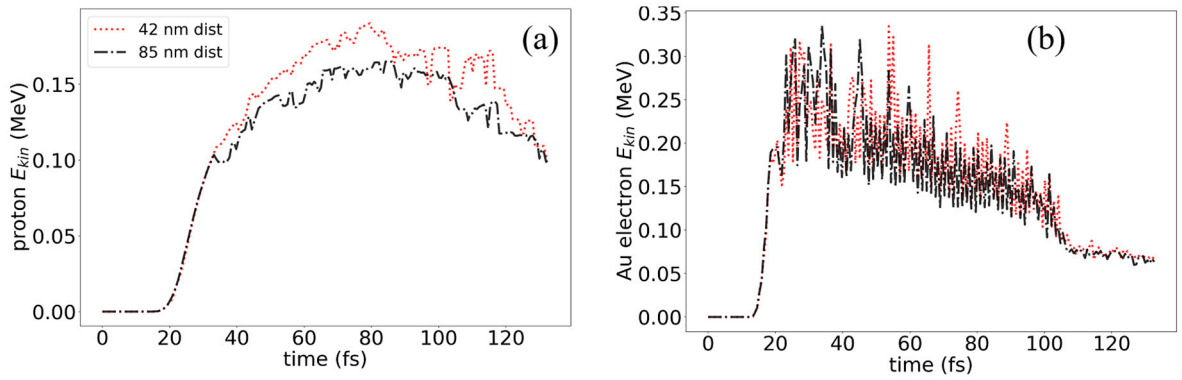

Figure 11. Proton energies (**a**) and electron energies (**b**) achieved in hydrogen-rich media with a resonating double dipole antenna pair separated by a 42 nm distance (red dashed line) and 85 nm (black dot-dashed line) upon irradiation of 4×10^{18} W/cm^2 intense laser pulse.

Closely spaced antenna pairs exhibit enhanced proton acceleration due to strong near-field coupling and plasmon hybridization between neighboring structures. At separations on the order of half a wavelength, constructive radiative coupling enhances the local field amplitude.

At quarter effective wavelength distances, the interaction becomes dominated by gap plasmon modes that produce extreme field confinement and amplification. These coupled modes distribute oscillatory currents across both antennas and delay the depletion of conduction electrons, thereby sustaining resonant behavior under intense irradiation.

As a result, bipolar charge-separation fields form in the inter-antenna gap, efficiently ionizing hydrogen and accelerating protons over extended timescales. Crossed and three-dimensional crossed antenna pairs further amplify these effects by supporting multiple hybridized plasmonic modes and larger near-field volumes, leading to systematically higher proton energies.

Our simulations show that the optimal spacing between coupled antennas is approximately one quarter of the resonant length, corresponding to about 40 nm.

We found that rod antenna arrays and multi-structure enhance the energies of protons due to several cooperative effects, such as the enhanced uniformity of field hotspots, overlapping plasmonic regions that create a combined effective enhancement, and multi-front proton acceleration that increases proton density. The two-sided counter-propagating laser irradiation and possibly multi-sided laser illumination for 3D antenna structures, such as 3D crossed antennas, further enhance proton energies, as illustrated in Figure 12, where the examples of a dipole, 2D cross, and 3D cross antenna shapes are compared.

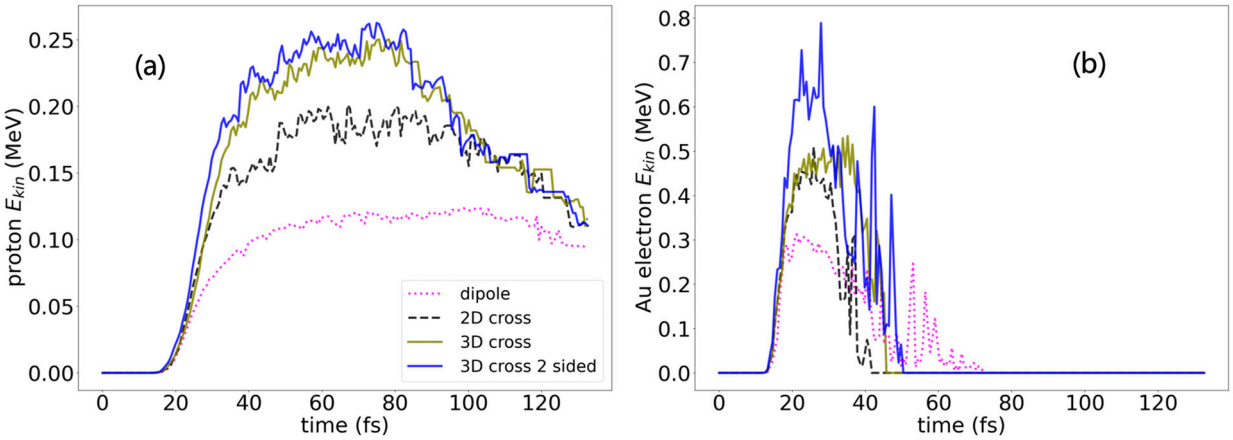

Figure 12. Effect of two-sided laser shot on the proton energies (**a**) and electron energies (**b**) of three-dimensional crossed antennas in comparison with that of a dipole and plain cross in a strong laser field of 4×10^{18} W/cm^2. See legend for antenna types.

It is worth noting that with periodic boundary conditions for the particles, the electrons remain in the simulation box, contrary to the simulation with open boundaries, when electrons are rapidly expelled by intense laser radiation. In the case of closed boundaries, the electron energies reached several MeV in the strong 4×10^{18} W/cm^2 laser field in the middle of the pulse duration, which is one-order-of-magnitude-higher energy than that with open boundaries in Figures 11b and 12b. However, proton energies did not increase further and remained at their maximum values, as shown in Figures 11a and 12a.

Adding a second counter-propagating laser pulse improves the symmetry of proton acceleration and enhances both the stability of the charge-separation field and the uniformity of the ion-energy distribution. Cross-based and double Yagi antennas benefit the most from this configuration of a double laser shot, as their geometry allows the full utilization of incident fields. Also, note the extended time for the electron energy gains in the right plot in Figure 12, which indicates the extended plasmon lifetime due to its confinement around the antenna in a symmetric opposite-sided laser shot, which does not blow away the knocked-out electrons so easily as one-sided radiation does.

When introducing a closely placed antenna pair in hydrogen-rich matter, a higher energy value can be achieved for ions upon irradiation using an intense laser field. As for closely placed dipoles, the proton energy rises to 200 keV; for a close pair of planar crosses, the proton energy is ≈250 keV; while a pair of closely placed 3D crosses (double 3D cross) accelerates protons to ≈350 keV for a pair with a distance of 85 nm and to ≈400 keV for a pair with a distance of 40 nm. This energy is higher than that for protons with a symmetric five-element Yagi-type antenna. The details will be addressed in a dedicated forthcoming publication.

The pronounced acceleration enhancement observed in coupled antennas motivates a detailed analysis of the physical mechanisms responsible for this behavior.

6. Discussion and Conclusions

The following discussion provides a mechanistic interpretation of the numerical observations, linking antenna geometry and spacing to plasmonic coupling, charge separation, and ion acceleration processes.

The present PIC approach is intended to describe strongly driven, ultrafast nonequilibrium dynamics in nanoantenna-doped media. While equilibrium nanoplasmonic phenomena at sub-10 nm scales may require nonlocal and quantum corrections, the extreme excitation regime considered here is dominated by collective particle–field dynamics, rapid ionization, and electron escape. The model therefore captures the primary mechanisms governing transient plasmon formation and decay, while detailed band-structure effects are beyond the present scope.

In our study, we numerically examined the ionization of hydrogen-rich matter with resonating antenna dopes of various shapes irradiated by infrared laser shots from one and two opposite sides with comprehensive intensity values in the range of ~10^{17}–10^{19} W/cm^2. We found significant differences in the maximum energies of protons for different antenna geometries and different laser shot setups. In particular, we found that the cross-based antennas outperformed the dipole rods. The superiority of crossed antennas arises from:

- Multi-directional current pathways.
- Geometric redundancy against polarization misalignment.
- Increased number of plasmonic modes.
- More resilient electron retention.
- Denser localized hotspots.

We found the limitations of nanoantennas at extreme intensities beyond ~10^{18} W/cm^2 in terms of the ionization of matter and proton energies achieved. These limitations primarily arise in extreme fields, when conduction electrons are expelled early, and the plasmonic enhancement collapses, causing the proton energies to plateau. This phenomenon fundamentally limits achievable energy gain.

In our comprehensive particle-in-cell simulations of the laser shot interaction with gold nanoantennas in dense hydrogen media, we obtained the following achievements:

- Model Validation: PIC methods successfully validated against traditional approaches.
- Superior Configuration: 3D crossed nanoantennas demonstrate exceptional performance, the highest near-field enhancement, and less orientation-sensitive gains than dipole-based antennas.
- Microscopic Effects: electron spill-out and kinetic effects are crucial for accurate modeling.
- Intensity Scaling: Cross-quadruple and 3D cross-sextuple advantages increase at higher intensities.

The analysis of our numerical results yields the following findings, potentially relevant for exploratory nanoplasmonic-assisted fusion concepts:

- Multi-arm crossed and Yagi-type antennas sustain stronger field enhancement than dipoles.
- Three-dimensional crossed antennas yield higher isotropic field enhancement and ion acceleration values.
- Proton energies reach ~200 keV at moderate intensities of <10^{18} W/cm^2 and saturate at higher intensities at a range of ~300–400 keV dependent on antenna geometry. These energies remain below typical fusion-relevant thresholds over MeV; the present results should be interpreted as demonstrating trends in energy localization and coupling rather than direct fusion-grade ion acceleration.

https://doi.org/10.3390/particles9020051

- Early depletion of gold's conduction electrons and fast dense plasma formation limit plasmon resonance behavior and time windows at intensities above ~10^{18} W/cm^2, making much stronger intensities not useful.
- Double and multiple symmetric antenna arrays in combination with multisided laser shots retain the plasmon resonance between the neighboring elements, enhance near-field in between them, and extend plasmon lifetime.
- Cross-based antennas support multiple resonance modes and their hybridization; they sustain stronger fields and preserve plasmonic behavior for longer durations, leading to the most efficient proton acceleration.

Complex antenna structures support multiple modes. Paired dipoles and Yagi-type antennas benefit from plasmon confinement between the resonating elements. Multiple crossed resonating elements of 3D antennas create many hybridized modes; multiple gap regions in coupled structures form simultaneously. This results in multiple high-acceleration spots, high effective acceleration volumes, multiple proton acceleration channels, and eventually higher total ion energy yields.

We next explain the reasons why the highest proton energies were observed for antenna separations of about 40 nm. A detailed investigation reveals that near-field plasmon hybridization between antennas plays a decisive role. When two nanoantennas are placed within a distance comparable to their near-field decay length, their plasmon modes no longer behave independently. Instead, they hybridize into bonding and antibonding plasmonic states, analogous to molecular orbitals.

At half-wavelength separation, antennas couple primarily through radiative fields, producing constructive dipolar interference. In contrast, at sub-50 nm separations near-field coupling dominates and generates extremely strong localized fields in the inter-antenna gap. This hybridization increases local electric-field amplitudes, enhances energy confinement, and strengthens field gradients driving ion acceleration.

The hybridized plasmonic response naturally leads to the formation of strongly confined gap modes at sufficiently small antenna separations. A key mechanism responsible for this behavior is gap-mode field enhancement. At separations of about 40 nm or less, a gap plasmon mode forms between the antennas. In this regime, oppositely charged surfaces face each other across a narrow gap, producing strong electric-field confinement and amplification. Field amplitudes scale approximately inversely with gap size and can exceed those of isolated antenna tips. Consequently, hydrogen in the gap is ionized extremely efficiently and strong charge-separation fields are generated once electrons are expelled. Protons originating near the gap therefore experience the strongest acceleration. In addition to field amplification, coupled antennas also exhibit modified temporal dynamics of the resonant response.

In contrast, the wider separation of antennas in a pair at $\lambda/2$ distance yields some larger areas for ion acceleration; thus, a higher number of protons can be accelerated to lower energies in comparison with the antennas place at a distance of $\lambda/4$.

Another important factor is the extended lifetime of resonance responses in coupled antennas. For isolated antennas, resonance collapses once conduction electrons are removed. In antenna pairs, hybridized plasmon modes distribute oscillatory currents across both elements. Electron depletion from one antenna can therefore be partially compensated by currents in the neighboring antenna, allowing the coupled system to behave as a larger effective resonator. This mechanism delays plasmon quenching and increases the effective acceleration time, resulting in higher proton energies. The extended plasmon lifetime is accompanied by characteristic charge-separation geometry that further enhances ion acceleration.

The constructive charge-separation geometry of paired antennas further contributes to proton acceleration. Closely spaced antennas generate a strong bipolar electric-field structure. Electrons are expelled outward from the gap region while a positive charge builds up on both antennas. This creates a large and sustained electric field within the gap that accelerates protons away from its center. Because these acceleration fields persist for longer than in single-antenna systems, ion motion remains coherent over larger distances and energy transfer becomes more efficient.

Another process contributing to resonance stabilization in coupled antennas is electron recirculation between neighboring elements. Electron recirculation also plays an important role in coupled antennas. In isolated antennas, electrons expelled into free space rapidly disrupt resonance. In contrast, closely spaced pairs allow electrons emitted from one antenna to be partially trapped by the field of the neighboring antenna. This recirculation maintains a higher local electron density near the antennas and stabilizes the plasmonic response. The delayed depletion of conduction electrons therefore postpones proton–energy saturation when increasing laser intensity.

Beyond particle dynamics, the spatial symmetry of the electromagnetic fields in paired antennas also influences energy localization efficiency. Field symmetry contributes to the improved performance of paired antennas. Such geometries produce more symmetric field distributions, reduce radiation losses, and enhance near-field confinement. This increases the fraction of laser energy stored locally rather than radiated away, providing higher local energy density for ionization and acceleration.

The above discussion can be summarized in Table 1, where we show that the effect is stronger in ~40 nm coupled antennas rather than half-wavelength distant pairs.

Table 1. Summary of coupled antennas' distance separation effects on the fields and proton energy.

Separation	Dominant Coupling	Effect on Proton Energy
$\sim\lambda/2$	Far-field (radiative)	Moderate enhancement
~40 nm	Near-field (gap plasmon)	Strong enhancement
<20 nm	Quantum effects (not modeled)	Beyond PIC validity

As the numerical modeling is classic and does not extend to quantum effects, we found that ~40 nm coupled nanoantennas were the optimal. At this distance:

- Coupling is purely classical and strong.
- PIC scheme remains valid.
- Gap fields are maximized without entering tunneling regimes.

The demonstrated capability of plasmonic nanoantenna systems to concentrate laser energy and accelerate ions suggests potential applications in advanced laser–matter interaction regimes.

Our findings highlight the importance of geometry in designing nanoengineered targets for advanced laser–matter interaction and prospective fusion concepts, and motivate future work exploring larger arrays, broadband excitation, and antenna materials with slower electron depletion. With regard to the nanoplasmonic-enhanced ICF, our results support the idea that nanoantennas embedded into an ICF ablator or fuel enhance local absorption may contribute to ignition-assisting mechanisms through improved localized energy deposition and improve the uniformity of laser coupling. Properly coupled multi-element crossed- and Yagi-based antennas are especially attractive candidates due to their geometric features and stability of resonance between the elements. A short summary of the conclusions can be found in Table 2.

Table 2. Summary table of antenna types.

DIPOLE	CROSS-BASED ANTENNAS	YAGI ANTENNAS
Orientation dependent; simpler geometry	Multi-directional, robust, stronger enhancement	Directed geometry, strong hotspots
Proton energies: ~100–120 keV	Proton energies: ~180–250 keV	Proton energies: ~200–300 keV
Resonance collapses faster	Longer plasmon lifetime; hybrid modes	Efficient multi-element coupling

Author Contributions: Conceptualization, K.Z. and I.P.; methodology, K.Z.; software, I.P.; validation, K.Z. and I.P.; formal analysis, K.Z.; investigation, K.Z. and I.P.; resources, K.Z. and I.P.; data curation, I.P.; writing—original draft preparation, K.Z.; writing—review and editing, K.Z. and I.P.; visualization, K.Z. and I.P.; supervision, K.Z. and I.P. All authors have read and agreed to the published version of the manuscript.

Funding: The author K. Zsukovszki acknowledges support from the Hungarian Office for Research, Development and Innovation (NKFIH) under project number 2022-2.1.1-NL-2022-00002 and from the project NKFI-Advanced 150038.

Data Availability Statement: The original contributions presented in this study are included in the article. Further inquiries can be directed to the corresponding author.

Conflicts of Interest: The authors declare no conflict of interest.

References

1. Tanabe, K. *Plasmonics for Hydrogen Energy*; Springer: Berlin/Heidelberg, Germany, 2022.
2. Purvis, M.A.; Shlyaptsev, V.N.; Hollinger, R.; Bargsten, C.; Pukhov, A.; Prieto, A.; Wang, Y.; Luther, B.M.; Yin, L.; Wang, S.; et al. Relativistic plasma nanophotonics for ultrahigh energy density physics. *Nat. Photonics* **2013**, *7*, 796–800. [CrossRef]
3. Chlouba, T.; Shiloh, R.; Kraus, S.; Brückner, L.; Litzel, J.; Hommelhoff, P. Coherent nanophotonic electron accelerator. *Nature* **2023**, *622*, 476–480. [CrossRef] [PubMed]
4. Xie, R.; Cao, L.H.; Chao, Y.; Jiang, Y.; Liu, Z.J.; Zheng, C.Y.; He, X.T. Improvement of laser absorption and control of particle acceleration by subwavelength nanowire target. *Phys. Plasmas* **2020**, *27*, 123108. [CrossRef]
5. Kong, D.; Zhang, G.; Shou, Y.; Xu, S.; Mei, Z.; Cao, Z.; Pan, Z.; Wang, P.; Qi, G.; Lou, Y.; et al. High-energy-density plasma in femtosecond-laser-irradiated nanowire-array targets for nuclear reactions. *Matter Radiat. Extrem.* **2022**, *7*, 064403. [CrossRef]
6. Shiloh, R.; Chlouba, T.; Yousefi, P.; Hommelhoff, P. Particle acceleration using top-illuminated nanophotonic dielectric structures. *Opt. Express* **2021**, *29*, 14403–14411. [CrossRef] [PubMed]
7. Kern, C.; Zürch, M.; Petschulat, J.; Pertsch, T.; Kley, B.; Käsebier, T.; Hübner, U.; Spielmann, C. Comparison of femtosecond laser-induced damage on unstructured vs. nano-structured Au-targets. *Appl. Phys. A* **2011**, *104*, 15. [CrossRef]
8. Halas, N. Playing with Plasmons: Tuning the Optical Resonant Properties of Metallic Nano shells. *MRS Bull.* **2005**, *30*, 362–367. [CrossRef]
9. Bardhan, R.; Grady, N.K.; Ali, T.; Halas, N.J. Metallic Nanoshells with Semiconductor Cores: Optical Characteristics Modified by Core Medium Properties. *ACS Nano* **2010**, *4*, 6169–6179. [CrossRef]
10. Passoni, M.; Sgattoni, A.; Prencipe, I.; Fedeli, L.; Dellasega, D.; Cialfi, L.; Choi, I.W.; Kim, I.J.; Janulewicz, K.A.; Lee, H.W.; et al. Toward high-energy laser-driven ion beams: Nanostructured targets. *Phys. Rev. Accel. Beams* **2016**, *19*, 061301. [CrossRef]
11. Chen, Y.; Wu, H.; Li, Z.; Wang, P.; Yang, L.; Fang, Y. The Study of Surface Plasmon in Au/Ag Core/Shell Compound Nanoparticles. *Plasmonics* **2012**, *7*, 509–513. [CrossRef]
12. Kelly, K.L.; Coronado, E. The optical properties of metal Nanoparticles: The influence of size, shape, and dielectric environment. *J. Phys. Chem. B* **2003**, *107*, 668–677. [CrossRef]
13. Link, S.; El-Sayed, M.A. Spectral Properties and Relaxation Dynamics of Surface Plasmon Electronic Oscillations in Gold and Silver Nanodots and Nanorods. *J. Phys. Chem. B* **1999**, *103*, 8410. [CrossRef]
14. Zsukovszki, K.; Papp, I. Numerical Study of Ionization Dynamics in Matter with Gold Nanoparticles Upon Laser Irradiation of Various Intensities. *Particles* **2025**, *8*, 27. [CrossRef]
15. Zsukovszki, K.; Papp, I. Numerical analysis of ionization and plasmonic phenomena on gold nanodopes upon laser pulse irradiation. *Results Phys.* **2025**, *72*, 108198. [CrossRef]

16. Zsukovszki, K.; Papp, I. Ionization of matter with resonating nanoantennas under intense laser irradiation—Numerical study. *Rad. Phys. Chem.* **2025**, *237*, 113111. [CrossRef]
17. Papp, I.; Zsukovszki, K. Particle simulation of various gold nanoantennas in laser-irradiated matter for fusion production. *Eur. Phys. J. Spec. Top.* **2025**, *234*, 2993–2998. [CrossRef]
18. Zsukovszki, K.; Papp, I. Comparative Analysis of Optical Absorption and Resonating Dynamics of Nanoantenna Dopes at Intense Laser Shots. *Eur. Phys. J. Spec. Top.* **2025**, *234*, 3021–3028. [CrossRef]
19. Papp, I.; Bravina, L.; Csete, M.; Kumari, A.; Mishustin, I.N.; Motornenko, A.; Rácz, P.; Satarov, L.M.; Stöcker, H.; Strottman, D.D.; et al. Kinetic model of resonant nanoantennas in polymer for laser induced fusion. *Front. Phys.* **2023**, *11*, 1116023. [CrossRef]
20. Bonyár, A.; Szalóki, M.; Borók, A.; Rigó, I.; Kámán, J.; Zangana, S.; Veres, M.; Rácz, P.; Aladi, M.; Kedves, M.Á.; et al. The Effect of Femtosecond Laser Irradiation and Plasmon Field on the Degree of Conversion of a UDMA-TEGDMA Copolymer Nanocomposite Doped with Gold Nanorods. *Int. J. Mol. Sci.* **2022**, *23*, 13575. [CrossRef] [PubMed]
21. Kroo, N.; Csernai, L.P.; Papp, I.; Kedves, M.A.; Aladi, M.; Bonyár, A.; Szalóki, M.; Osvay, K.; Varmazyar, P.; Biró, T.S.; et al. Indication of $p+{}^{11}$B reaction in Laser Induced Nanofusion experiment. *Sci. Rep.* **2024**, *14*, 30087. [CrossRef]
22. Chubchev, E.D.; Vladimirova, Y.V. Near-field polarization of a plasmonic prolate nanospheroid in a Gaussian beam. *Laser Phys. Lett.* **2015**, *12*, 015302. [CrossRef]
23. Pastukhov, V.M.; Vladimirova, Y.V.; Zadkov, V.N. Photon-number statistics from resonance fluorescence of a two-level atom near a plasmonic nanoparticle. *Phys. Rev. A* **2014**, *90*, 063831. [CrossRef]
24. Arber, T.D.; Bennett, K.; Brady, C.S.; Lawrence-Douglas, A.; Ramsay, M.G.; Sircombe, N.J.; Gillies, P.; Evans, R.G.; Schmitz, H.; Bell, A.R.; et al. Contemporary particle-in-cell approach to laser-plasma modelling. *Plasma Phys. Control. Fusion* **2015**, *57*, 113001. [CrossRef]
25. Smith, J.R.; Orban, C.; Rahman, N.; McHugh, B.; Oropeza, R.; Chowdhury, E.A. A particle-in-cell code comparison for ion acceleration. *Phys. Plasmas* **2021**, *28*, 074505. [CrossRef]
26. Nuter, R.; Gremillet, L.; Lefebvre, E.; Lévy, A.; Ceccotti, T.; Martin, P. Field ionization models in particle-in-cell codes. *Phys. Plasmas* **2011**, *18*, 033107. [CrossRef]
27. Feng, W.; Schultz, J.; Wolf, D.; Pylypenko, S.; Gemming, T.; Weinel, K.; Jácome, L.A.; Büchner, B.; Lubk, A. Secondary electron emission from gold microparticles in a transmission electron microscope: Comparison of Monte Carlo simulations with experimental results. *J. Phys. D Appl. Phys.* **2025**, *58*, 085102. [CrossRef]
28. Available online: https://epochpic.github.io/#about (accessed on 22 February 2022).
29. Nanbu, K.; Yonemura, S. Weighted particles in Coulomb collision simulations based on the theory of a cumulative scattering angle. *J. Comput. Phys.* **1998**, *145*, 639. [CrossRef]
30. Pérez, F.; Gremillet, L.; Decoster, A.; Drouin, M.; Lefebvre, E. Improved modeling of relativistic collisions and collisional ionization in particle-in-cell codes. *Phys. Plasmas* **2012**, *19*, 083104. [CrossRef]
31. Boris, J.P. Relativistic plasma simulation-Optimization of a hybrid code. In Proceedings of the Fourth Conference on Numerical Simulation of Plasmas, Washington, DC, USA, 2–3 November 1970; pp. 3–67.
32. Villasenor, J.; Buneman, O. Rigorous charge conservation for local electromagnetic field solvers. *Comput. Phys. Commun.* **1992**, *69*, 306–316. [CrossRef]
33. Novotny, L. Effective Wavelength Scaling for Optical Antennas. *Phys. Rev. Lett.* **2007**, *98*, 266802. [CrossRef]
34. Maier, S.A. *Plasmonics: Fundamentals and Applications*; Springer Science and Business Media: New York, NY, USA, 2007.
35. Childs, H.; Brugger, E.; Whitlock, B.; Meredith, J.; Ahern, S.; Pugmire, D.; Biagas, K.; Miller, M.C.; Harrison, C.; Weber, G.H.; et al. *High Performance Visualization—Enabling Extreme-Scale Scientific Insight*; CRC Press: Boca Raton, FL, USA, 2012. [CrossRef]